8-6-2018

Unraveling the Structure and Bonding Evolution of the Newly Discovered Iron Oxide FeO2

Cheng Lu
University of Nevada, Las Vegas, cheng.lu@unlv.edu

Maximilian Amsler
Cornell University, amsler.max@gmail.com

Changfeng Chen
University of Nevada, Las Vegas; Tufts University School of Medicine, chen@physics.unlv.edu

Repository Citation

Lu, C., Amsler, M., Chen, C. (2018). Unraveling the Structure and Bonding Evolution of the Newly Discovered Iron Oxide FeO2. *Physical Review B, 95*(5), 1-7.
http://dx.doi.org/10.1103/PhysRevB.98.054102

Unraveling the structure and bonding evolution of the newly discovered iron oxide FeO_2

Cheng Lu,[1,*] Maximilian Amsler,[2,†] and Changfeng Chen[1,‡]
[1]*Department of Physics and High Pressure Science and Engineering Center, University of Nevada, Las Vegas, Nevada 89154, USA*
[2]*Laboratory of Atomic and Solid State Physics, Cornell University, Ithaca, New York 14853, USA*

(Received 23 May 2018; published 6 August 2018)

Recently reported synthesis of FeO_2 at high pressure has stimulated great interest in exploring this new iron oxide and elucidating its properties. Here, we present a systematic computational study of crystal structure, chemical bonding, and sound velocity of FeO_2 in a wide range of pressure. Our results establish thermodynamic stability of the experimentally observed pyrite phase (P-phase) of FeO_2 at pressures above 74 GPa and unveil two metastable FeO_2 phases in $Pbcn$ and $P4_2/mnm$ symmetry at lower pressures. Simulated x-ray diffraction (XRD) spectra of $Pbcn$ and $P4_2/mnm$ FeO_2 match well with measured XRD data of the decompression products of P-phase FeO_2, providing compelling evidence for the presence of these metastable phases. Energetic calculations reveal unusually soft O-O bonds in P-phase FeO_2 stemming from a low-frequency libration mode of FeO_6 octahedra, rendering the O-O bond length highly sensitive to computational and physical environments. Calculated sound-velocity profiles of P-phase FeO_2 are markedly different from those of the $Pbcn$ and $P4_2/mnm$ phases, underscoring their distinct seismic signatures. Our findings offer insights for understanding the rich structural, bonding, and elastic behaviors of this newly discovered iron oxide.

DOI: 10.1103/PhysRevB.98.054102

I. INTRODUCTION

Iron oxides constitute a considerable fraction of the Earth's composition [1–4] and have attracted great interest as prototypes for modeling the material behavior in Earth's deep interiors [2–5]. The phase diagram of the Fe-O system includes compounds of diverse stoichiometries, structures, and properties, which emerge at different pressure and temperature environments [6–12]. At ambient conditions, ferrous oxide (FeO, wüstite) [6] forms a paramagnetic Mott insulator in a rock-salt B1 structure, which undergoes a structural transition to a rhombohedral phase at 16 GPa. Hematite (α-Fe_2O_3) [7] is a wide-band antiferromagnetic insulator with a rhombohedral corundum-type structure, and its structural motif consists of stacked layers of corner-sharing octahedra with Fe atom surrounded by six O atoms. The Fe atom is not completely centered in the regular octahedron; instead, it is closer to three surrounding O atoms. Magnetite (Fe_3O_4) [8] is half-metallic with high spin polarization and mixed valence states, crystallizing in a cubic structure of the spinel $[Fe^{3+}]_A[Fe^{2+}Fe^{3+}]_BO_4$ type. Its tetrahedral four-coordinated A site is occupied by Fe^{3+}, while its octahedral six-coordinated B site is occupied by Fe^{2+} and Fe^{3+} [9]. At increasing pressure and temperature, additional phases of iron oxides have been reported, including Fe_4O_5 [10], Fe_5O_6 [11], Fe_5O_7, and $Fe_{25}O_{32}$ [12].

Recently, Hu *et al.* [4] reported the synthesis of a new phase of iron oxide, FeO_2, through a chemical reaction of Fe_2O_3 and O_2 at pressures above 75 GPa and a temperature of about 1600 K. Based on *in situ* XRD measurements and density functional theory (DFT) calculations, the authors suggested that FeO_2 adopts a crystal structure identical to pyrite (FeS_2), where O replaces S to form bonds with Fe and neighboring O atoms. In this structure, henceforth referred to as the P-phase, the corresponding lengths of the Fe-O and O-O bonds are reported to be 1.792 and 1.937 Å, respectively [13]. Consequently, Hu *et al.* [4] proposed to adopt a chemical picture typical for iron peroxide. Subsequent theoretical work [14], however, raised questions concerning the oxidation state of iron in FeO_2. Using DFT calculations, it was shown that the oxidation state of the Fe ions in the P-phase is not 2+, as in FeS_2, but has an unexpected valence close to 3+ based on the argument that the O-O distance in FeO_2 is much larger than in free O_2 molecules (1.21 Å) [15] or in $(O_2)^{2-}$ ions in typical peroxides (1.49 Å) [14,16]. Moreover, high-pressure evolution of the crystal structure and chemical bonding in FeO_2 and its impact on key physical properties remain largely unexplored.

To resolve fundamental structural and bonding behaviors of P-phase FeO_2, explore additional FeO_2 phases, and establish their structure and property evolution under pressure, we have performed an unbiased structure search by the Crystal structure AnaLYsis by Particle Swarm Optimization (CALYPSO) method [17,18] which has worked well on a large variety of materials [19–29], to determine the pressure-induced structural evolution and phase transition of FeO_2, accompanied by first-principles calculations [30–35] to probe associated energetics, chemical bonding, and elastic properties. In agreement with the experimental reports [4], our calculations identify the pyrite structure as the thermodynamically stable form of FeO_2 at pressures above 74 GPa. Our structure search also uncovers two metastable FeO_2 phases in $Pbcn$ and $P4_2/mnm$ symmetries at reduced pressures. An analysis of simulated and measured XRD spectra shows a good match between these metastable phases and the decompression products of FeO_2 obtained in

*cheng.lu@unlv.edu
†amsler.max@gmail.com
‡chen@physics.unlv.edu

the experiment [4]. Our energetic calculations unveil that the O-O bonding in FeO_2 is unusually soft, which is attributed to a low-frequency libration mode of FeO_6 octahedra, making the O-O bond length highly sensitive to computational (e.g., types of exchange-correlation potential and whether or not including the onsite Coulomb interaction) and physical (e.g., pressure and temperature) environments. We also calculated elastic parameters to determine the sound velocities of the identified FeO_2 phases to assess their seismic signatures.

II. COMPUTATIONAL METHODS

Our structure prediction is based on a global optimization of the free-energy surfaces using the CALYPSO methodology [17,18], which has the capability of predicting crystal structures with only the knowledge of the chemical composition at given external conditions (for example, pressure) as input [24–29]. In this work, the variable-cell approach is used with one to four formula units (f.u.) of FeO_2, and a fixed-cell approach with one, two, and four FeO_2 f.u. per cell. Structural searches are performed at 0, 25, 30, 40, 50, 75, 100, and 150 GPa. Nonmagnetic (NM) DFT calculations are adopted in the variable-cell structure searches, while spin-polarized DFT + U calculations are adopted in the fixed-cell structure searches. Each generation of trial structures contains 50 candidates, with 70% generated by the particle swarm optimization (PSO) and 30% generated randomly; the search is terminated after 30 generations. The top 50 structures with relatively low-energy in the CALYPSO structure searches are reoptimized by spin-polarized DFT + U calculations to identify the true ground-state structures of FeO_2 under different pressures.

The underlying first-principles structural relaxations and electronic property calculations are carried out using DFT with the Perdew-Burke-Ernzerhof (PBE) exchange-correlation functional as implemented in the VASP code [30]. To take into account electronic correlation effects, we include an onsite Coulomb repulsion term within the generalized gradient approximation (GGA + U) [36–38]. The frozen-core all-electron projector-augmented wave (PAW) method [31] is adopted, with $3d^7 4s^1$ and $2s^2 2p^4$ treated as valence electrons for Fe and O, respectively. A cutoff energy of 800 eV for the expansion of the wave function into plane waves and fine Monkhorst-Pack k meshes [32] is chosen to ensure that the enthalpies are converged to better than 1 meV/atom.

The enthalpy-pressure relations of FeO_2 are calculated using the GGA + U functional. We adopted the optimized values for U (5 eV; onsite Coulomb interaction) and J (0.8 eV; Hund coupling constant) from a recent work [39] to describe the electronic structure of FeO_2. The decomposition ($Fe_2O_3 + O_2$) enthalpies are calculated by adopting the α-Fe_2O_3, ζ-Fe_2O_3, ι-Fe_2O_3, and η-Fe_2O_3 structures for Fe_2O_3 [12], and α-O_2, δ-O_2, ε-O_2, and ζ-O_2 structures for solid oxygen [40]. For example, at 75 GPa, the ground-state structures of Fe_2O_3 and O_2 are η-Fe_2O_3 ($Cmcm$ symmetry) and ε-O_2 ($C2/m$ symmetry), respectively. The decomposition enthalpies of Fe_2O_3 and O_2 at 75 GPa are calculated by considering η-Fe_2O_3 and ε-O_2 structures, which results in the $Fe_2O_3 + O_2$ data line. For comparison with the experimental data, we also performed the pressure-volume calculations by using other exchange-correlation functionals, including the generalized gradient approximation (GGA), the local density approximation (LDA), and LDA + U.

The phonon calculations are carried out using the supercell approach [41] as implemented in the PHONOPY code [33]. Electronic charges are calculated using Bader's quantum theory of atom in molecules approach [34] with a $300 \times 300 \times 300$ fast Fourier transform grid. The crystal orbital Hamilton population (COHP) analysis is performed using the LOBSTER package [35]. Both the Bader charge analysis and the COHP analysis are based on spin-polarized DFT + U calculations. The elastic-wave velocities are determined by solving the Cristoffel equation, defined as $\det|T_{ik} - \delta_{ik}\rho V^2| = 0$, where δ_{ik} is the Kronecker delta function, V is one of the seismic velocities, and T_{ik} is the Christoffel stiffness [42].

III. STRUCTURE EVOLUTION

We have performed a systematic structure search using fixed and variable cells that contain up to four formula units in the pressure range of 0–150 GPa. The pressure evolution of the enthalpies for the relevant encountered phases is shown in Fig. 1(a). At 0 GPa, all examined FeO_2 structures are unstable against dissociation into Fe_2O_3 and O_2, consistent with the experimental observation that no crystalline FeO_2 phase is seen at ambient conditions. The enthalpy of P-phase FeO_2 decreases quickly with rising pressure and drops below that of Fe_2O_3+O_2 at 74 GPa, which is in excellent agreement with the experimental transition pressure of 75 GPa [4]. Our results show that P-phase FeO_2 remains the stable structure up to 150 GPa. Interestingly, upon decompression below 74 GPa, the enthalpy of P-phase FeO_2 intersects with those of three nearly degenerate metastable FeO_2 phases, in $P4_2/mnm$, $Pbcn$, and $P2/m$ symmetries, respectively, that coexist in the pressure range of 30–40 GPa and are dynamically stable as evidenced by their calculated phonon dispersion curves that show no imaginary phonon modes [Fig. 1(b)]. This raises an intriguing possibility of finding new FeO_2 phases in the decompression products of the P-phase provided the kinetic barrier for the dissociation is sufficiently high. The metastable FeO_2 phase in $P4_2/mnm$ symmetry is isomorphous with the rutile phase of TiO_2, which is among the most commonly observed structure types for transition-metal dioxides, including CrO_2 and MnO_2 [43,44]. The metastable FeO_2 phase in orthorhombic $Pbcn$ symmetry adopts an α-PbO_2-type structure. We list in Table S1 of the Supplemental Material [45] the structural details of the stable P-phase and three metastable phases of FeO_2 at select pressure points where experimental measurements were taken and comparisons made (see below) with calculated results.

We have simulated XRD spectra of all four FeO_2 phases shown in Fig. 1(b) and compared the results with experimental XRD data. We find an excellent match between simulated and experimental XRD data at 76 GPa [Fig. 2(a)]. Meanwhile, in the absence of decomposition into Fe_2O_3 and O_2, the pressure evolution of the predicted metastable FeO_2 phases can be regarded as a sequence of phase transitions on decompression. To verify this conjecture, we have obtained from the authors of the experimental work [4] their unpublished high-resolution XRD data taken at 31 and 41 GPa, where our calculated enthalpy results [Fig. 1(a)] show that P-phase and metastable FeO_2 phases become very close in enthalpy and, therefore,

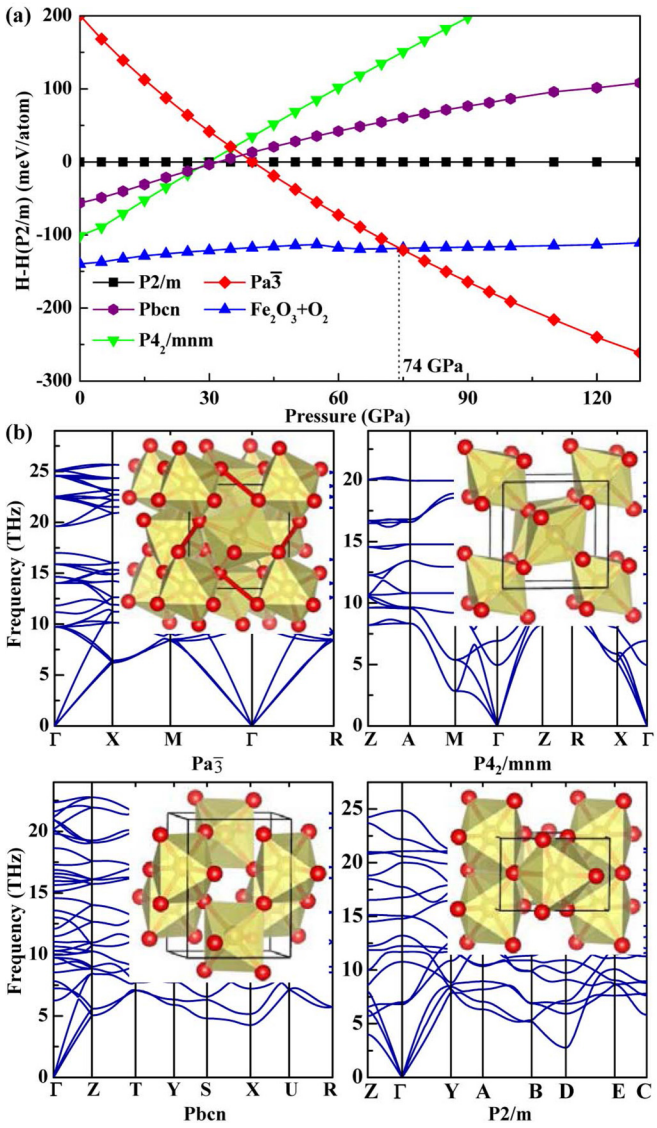

FIG. 1. (a) Calculated enthalpy-pressure relations of four FeO_2 phases compared to decomposition products Fe_2O_3+O_2. (b) Calculated phonon dispersion curves of the four FeO_2 phases (their crystal structures presented in insets) that show no imaginary modes, confirming their dynamic stability.

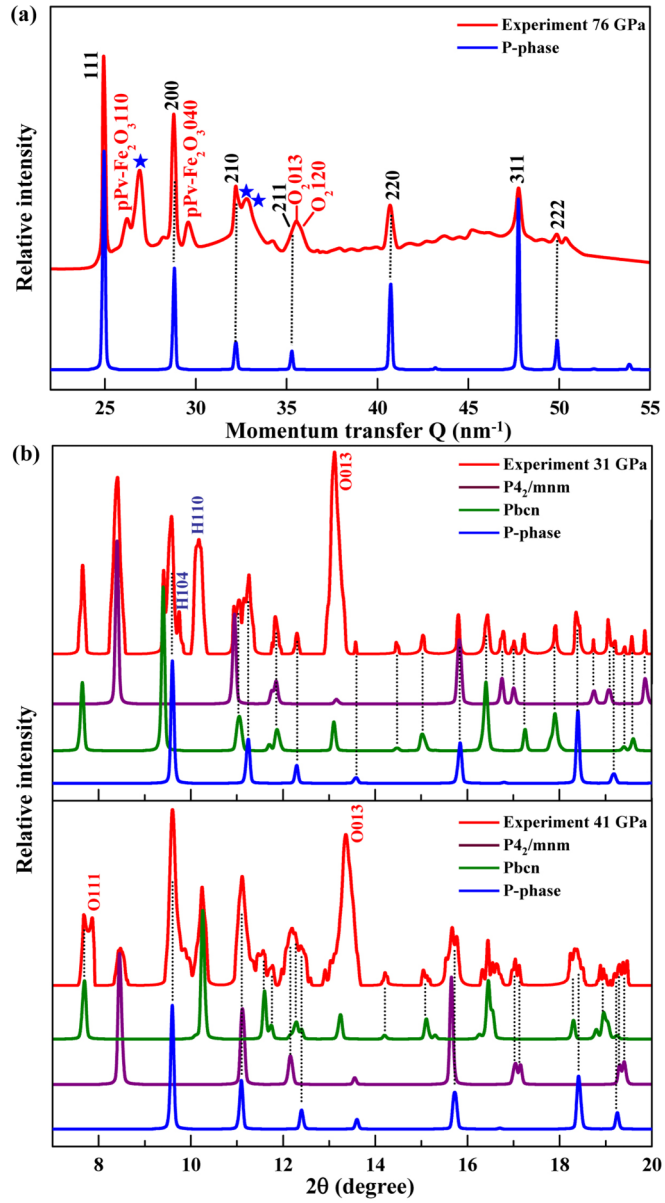

FIG. 2. Simulated and measured [4] XRD patterns of FeO_2 at (a) 76 GPa, where P-phase FeO_2 is well established and at (b) 31 and 41 GPa, where metastable FeO_2 phases in $P4_2/mnm$ and $Pbcn$ symmetry are clearly identified to coexist with the P-phase. The x-ray wavelength is 0.4344 Å in both cases.

are likely to coexist. A comparison of the simulated and measured XRD spectra [Fig. 2(b)] indeed shows that nearly all of the previously unassigned and unexplained diffraction peaks that appear but do not match the spectra of P-phase FeO_2 at 31 and 41 GPa find excellent matches with the simulated XRD peaks of the $P4_2/mnm$ and $Pbcn$ FeO_2 phases. This remarkable match indicates the likely presence of these two metastable phases in the decompression product. Meanwhile, the simulated XRD peaks of the $P2/m$ FeO_2 phase (not shown here) are absent in the measured XRD spectra, probably impeded by a higher-energy barrier associated with this particular phase transition. These findings offer compelling evidence for the existence of the metastable FeO_2 phases in $P4_2/mnm$ and $Pbcn$ symmetry within the range of the experimentally probed pressures, i.e., 31 to 41 GPa. These phases likely exist in an even wider range of pressure, but more work is needed to gain insight regarding their phase boundaries, which is an interesting topic for further study, especially at the low-pressure end where the $P4_2/mnm$ phase has a clear energetic advantage and may become a single phase in the recovered specimen. The presence of these metastable phases at reduced pressures establishes viable FeO_2 crystal structures, which have important implications for expanding the iron oxide family of compounds and assessing their impact on geophysical and geochemical processes.

IV. CHEMICAL BONDING AND VALENCE STATE

We have explored several exchange-correlation functionals and different types of pseudopotentials to examine how these

different computational environments affect the energetic, structural, and electronic properties of FeO_2. We first examined lattice parameters of FeO_2 at 76 GPa. Experimental results show that P-phase FeO_2 is stable at this pressure with an observed lattice parameter of $a = 4.3640$ Å and a volume of $V = 83.115$ Å^3. We adopted the structure of P-phase FeO_2 and atomic positions from the extended Data Table 2 of Hu *et al.* [4] and performed structural relaxations at 76 GPa using different DFT methods. The semilocal PBE functional with the standard PAW potentials in a closed-shell setting produces an O-O bond length of 2.066 Å, agreeing well with previously reported [4] theoretical O-O distance of 2.077 Å. We find only minor changes in the structural parameters when using the hard/semicore PAW potentials provided in VASP [30].

We then examined the electronic correlation effect within the GGA + U approach [36–38]. We adopted the recently proposed [39] onsite Coulomb interaction term $U = 5$ eV and Hund coupling parameter $J = 0.8$ eV for Fe. Within different magnetic states used in the calculations, *we find large variations of the O-O distances, ranging from 1.876 to 2.232 Å.* The calculated O-O distance is 1.876 Å in the GGA + U approach without spin polarization, which agrees well with the theoretical O-O bond length of 1.896 Å reported by Jang *et al.* [13]. On the other hand, a spin-polarized calculation shows that an antiferromagnetic (AFM) state lowers the total energy compared to the closed-shell or ferromagnetic (FM) setting, leading to an O-O distance of 2.232 Å. This low-energy AFM spin state has alternating spin-up and spin-down Fe layers, which breaks the cubic symmetry and leads to an orthorhombic cell with the lattice parameters of $a = 4.3683$ Å, $b = 4.3621$ Å, and $c = 4.3613$ Å, which are very close to the lattice constant of $a = 4.3639$ Å in a symmetrized cubic cell with a volume of 83.104 Å^3, and the same as the experimental data ($a = 4.3640$ Å and $V = 83.115$ Å^3) at 76 GPa [4]. Further, the computed Fe-O bond length is 1.7873 Å, merely 0.29% shorter than the experimental value of 1.7925 Å. This good overall agreement between theory and experiment (see Supplemental Material, Table S2 [45]) indicates that the AFM GGA + U approach provides a good description of P-phase FeO_2, despite a notable discrepancy in an overestimation of the O-O distance at 2.2322 Å compared to the experimental value of 1.9371 Å [4]. We also calculated the volume-pressure relation for P-phase FeO_2, and the results also show that the GGA + U approach produces the best agreement with experimental data (Supplemental Material, Fig. S1 [45]).

To elucidate the sensitive nature of the O-O bond length under different computational environments, we investigated structural dynamics of FeO_2 by calculating its phonon dispersion at 76 GPa using a $2 \times 2 \times 2$ supercell. The results reveal a low-frequency transverse optical (TO) mode at about 11.8 THz at the Γ point, which corresponds to a rigid rotation of the FeO_6 octahedra. This libration eigenmode [see Fig. 3(a)] causes a stretching/shortening of the O-O bond. The large variation of the calculated bond lengths indicates a very soft energy landscape along the associated O-O dimer direction.

To evaluate the softness of the energy landscape for the O-O bonding in FeO_2, we compute its energy profile along the O-O stretching mode and compare with that of a typical peroxide (Na_2O_2) [46] and a simple oxide (RuO_2) [47]. At discrete, fixed

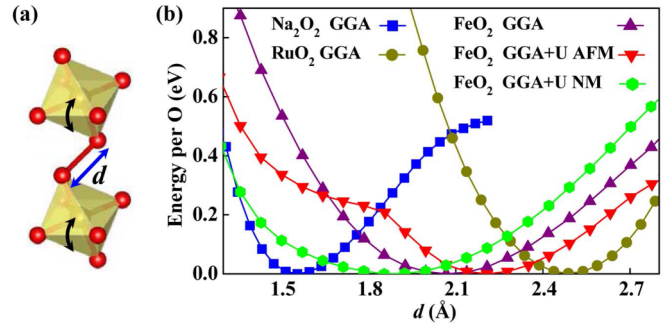

FIG. 3. (a) Illustration of the FeO_6 octahedra libration mode, indicated by the black double-arrow-headed lines, leading to the stretching/shortening, indicated by the blue double-arrow-headed line, of the O-O bond connecting adjacent octahedra. (b) Energy versus the O-O bond length d, as defined in (a), calculated using various functionals compared to the results of Na_2O_2 and RuO_2.

O-O bond lengths we allow the remaining atoms to relax, while keeping the cell parameters at their equilibrium values. This allows a mapping of the energy landscape as a function of the O-O distance. Results in Fig. 3(b) show that the equilibrium O-O distance in FeO_2 lies between that of Na_2O_2 (1.54 Å) and RuO_2 (2.49 Å), and that the curvature of the energy landscape along the O-O bond is much softer for FeO_2 compared to those of Na_2O_2 and RuO_2. In fact, the curvature for FeO_2 (between 0.77 and 1.57 eV/Å^2, depending on the exchange-correlation functional and the magnetic state used in the calculation) is significantly lower than the value for Na_2O_2 (4.58 eV/Å^2) or RuO_2 (2.66 eV/Å^2). Such softness of the O-O bond in FeO_2 explains its high sensitivity to computational environments and suggests that it also will be sensitive to actual physical environments, such as temperature and pressure, which vary at different synthesis, characterization, and geological conditions.

We have calculated electronic density of states (DOS) of the stable and metastable FeO_2 phases; the results (see Supplemental Material, Fig. S2 [45] for details) reveal metallic nature of the $P4_2/mnm$ and $Pbcn$ phases in the pressure range (31–41 GPa) of interest. In both cases, the DOS in the vicinity of the Fermi level has large contributions from the Fe $3d$ as well as the O $2p$ states, indicating a charge transfer between Fe $3d$ and O $2p$ orbitals. In contrast, the P-phase is semiconducting with an increasing band gap at rising pressure, reaching 0.481 eV at 76 GPa. We assess charge distribution in FeO_2 by computing the Bader charges using the atom in molecules approach [34,48–50], and the results show a considerable amount of charge transfer between Fe and O atoms. At 31 GPa, the Bader partial charges in the $P4_2/mnm$ phase are +1.76 and −0.88 for Fe and O, respectively. Similar values are found for the $Pbcn$ phase (+1.76 for Fe and −0.88 for O) and the P-phase (+1.75 for Fe and −0.875 for O) at the same pressure. The Bader charges of the P-phase at 76 GPa are reduced slightly to +1.60 and −0.80 for Fe and O, respectively. For comparison, the Fe Bader charges in other typical iron oxides at 76 GPa are +1.27 for FeO, +1.72 for Fe_2O_3, +1.72 and +1.47 for the two distinct Fe sites in Fe_3O_4. These results seem to suggest that the oxidation state of Fe in

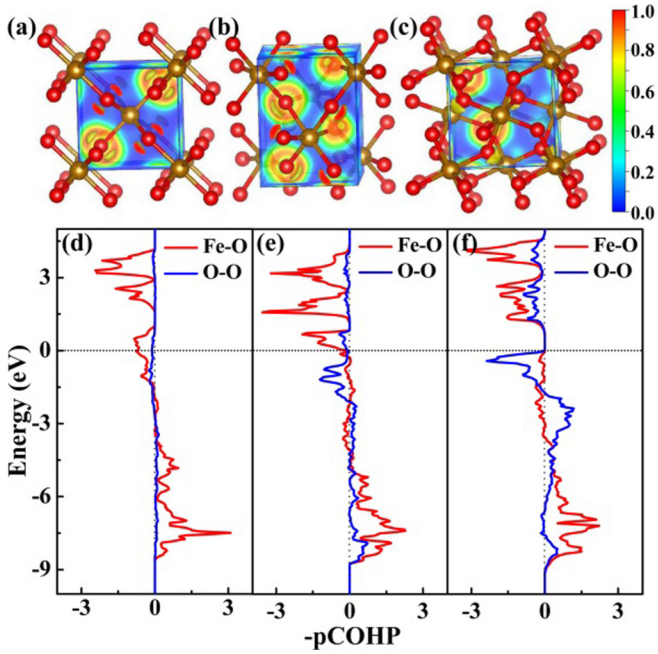

FIG. 4. ELF for select FeO_2 phases: (a) $P4_2/mnm$ at 31 GPa, (b) $Pbcn$ at 41 GPa, and (c) P-phase at 76 GPa. COHP for the Fe-O and O-O interactions in select FeO_2 phases: (d) $P4_2/mnm$ at 31 GPa, (e) $Pbcn$ at 41 GPa, and (f) P-phase at 76 GPa.

FeO_2 is close to 3+ since +1.60 is closer to +1.72 than +1.27. However, the calculated Bader charge of O in FeO_2 is −0.80, which is close to values in CaO_2 (−0.71/ − 0.74) and Na_2O_2 (−0.68/ − 0.70), and lower than those in FeO (−1.27), Fe_2O_3 (−1.14), and Fe_3O_4 (−1.15/ − 1.18) at 76 GPa. These findings support the picture that FeO_2 is a peroxide, in agreement with the initial interpretation of Hu *et al.* [4]. The oxidation state for Fe in FeO_2 is likely to attain a partial charge state $Fe^{+(2+\delta)}$, where δ ranges from 0 to 1 [51]. Further details on the charge states in FeO_2 and several other transition-metal oxides are given in the Supplemental Material, Table S3 [45].

We have further assessed the bonding character in FeO_2 by analyzing the electron localization function (ELF) [52], which provides a convenient measure to identify spatial localization of electrons, where values higher or lower than 0.5 represent regions with more or less electron localization compared to a uniform electron gas, respectively. The two metastable phases in $P4_2/mnm$ and $Pbcn$ symmetry show a strong localization of electrons in the vicinity of the O atom [Figs. 4(a) and 4(b)], which can be attributed to the O $2p$ lone electron pairs. At increasing pressure, small localized ELF basins form along the shortest O-O directions. Although the magnitude of this localization is small in the P-phase [Fig. 4(c)], it still indicates the formation of a single covalent bond between the nearest O atoms. The presence of this weak O-O covalent bond in the P-phase supports the picture that FeO_2 at 76 GPa is indeed a peroxide.

We also have performed a COHP [35,53–55] analysis to examine the difference in bonding properties between various FeO_2 phases. The COHP decomposes the DOS according to the weighted Hamiltonian matrix elements. Bonding and antibonding states are represented by positive and negative values of –COHP, respectively [56]. We show in Figs. 4(d)–4(f) select –COHPs of the shortest Fe-O and O-O bonds of $P4_2/mnm$, $Pbcn$, and P-phase FeO_2 at 31, 41, and 76 GPa, respectively. The Fe-O interactions look qualitatively similar in all three cases, with the occupied bonding states and unoccupied antibonding states below and above the Fermi level, respectively. The O-O interaction, on the other hand, varies significantly among the different phases. For the $P4_2/mnm$ phase [Fig. 4(d)], there is essentially no contribution from the O-O bonds in the COHP. For the $Pbcn$ phase at increased pressure, there is evidence of emerging O-O interaction [Fig. 4(e)] through the σ^* antibonding states slightly below the Fermi level (around −2 eV). This effect is stronger in the P-phase at further increased pressure, where the magnitude of the O-O antibonding states below the Fermi level has a sharp peak [Fig. 4(f)]. The integrated COHP (ICOHP) can provide an estimate of the strength of bonding. For comparison, we have calculated the ICOHP for the two adjoining O atoms in FeO_2. The ICOHP values are about −0.035 eV for $P4_2/mnm$ at 31 GPa, −0.121 eV for $Pbcn$ at 41 GPa, and −0.373 eV for P-phase at 76 GPa, respectively. Hence, the O-O σ^* antibonding interaction in the P-phase is stronger than in the other two phases. These results once again support the picture that the P-phase is a peroxide.

V. SOUND VELOCITY AND ANISOTROPY

We finally investigate the sound-velocity profile of the three viable FeO_2 phases and compare them to experimental results. Very recently, Liu *et al.* [5] measured the phonon density of states (PDOS) of FeO_2 by nuclear resonant inelastic x-ray scattering (NRIXS) technique at room temperature. The compressional (P wave, V_P) and shear (S wave, V_S) sound velocities of FeO_2 at 81(±2) GPa were 9.57 and 4.09 km/s, respectively. We have calculated the elastic tensors C_{11}, C_{12}, and C_{44}, and derived the V_P and V_S of P-phase FeO_2 at 81 GPa. The obtained sound velocities V_P (10.85 km/s) and V_S (5.95 km/s), are in reasonable agreement with the experimental values (see Supplemental Material, Table S4 [45]). The discrepancy between experiment and theory may be attributed to several factors, including the presence of hydrogen in the FeO_2 sample [4], the anharmonic effects [57] that were neglected in the calculations, and an orientational preference of the specimen caused by a uniaxial stress component in the sample chamber.

The intrinsic sound-velocity anisotropy defined by $AV_X = 100\% \times (V_{X\max} - V_{X\min})/[(X_{X\max} + X_{X\min})/2]$ $(X = P, S)$ describes the directional propagation of sound waves [42]. Results in Fig. 5(a) show that extremal P-wave propagations of $P4_2/mnm$ FeO_2 at 31 GPa occur in the basal plane with the fastest velocity ($V_{P\max} = 10.08$ km/s) in the ⟨001⟩ direction and the slowest ($V_{P\min} = 7.33$ km/s) in the $\langle\bar{1}00\rangle$ direction. The corresponding AV_P and AV_S are 31.5% and 77.02%, respectively. The fastest and slowest V_P of $Pbcn$ FeO_2 at 41 GPa are 10.54 km/s in the ⟨230⟩ direction and 8.23 km/s in the ⟨100⟩ direction, respectively, with an AV_P of 24.6% [Fig. 5(b)]. The maximum AV_S is 33.55% in the ⟨302⟩ direction, a reduction by half compared to the value for the $P4_2/mnm$ phase.

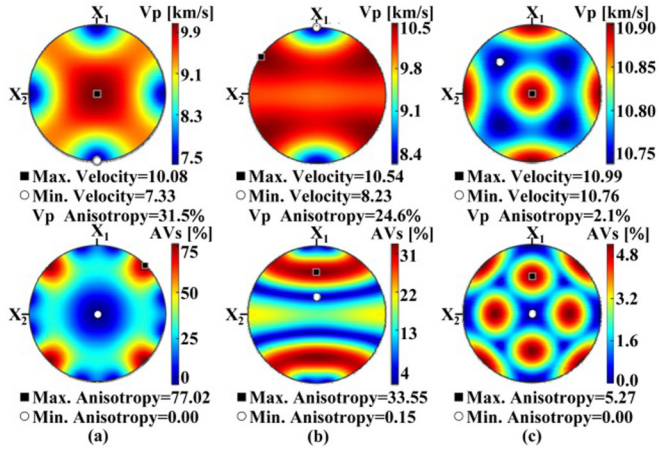

FIG. 5. Stereographic projections of calculated P-wave velocity V_P (in km/s) and S-wave anisotropy AV_S (in %) for (a) $P4_2/mnm$ FeO_2 at 31 GPa, (b) $Pbcn$ FeO_2 at 41 GPa, and (c) P-phase FeO_2 at 81 GPa. The coordinate axes are $X_1 = [100]$, $X_2 = [010]$, $X_3 = [001]$. The black square (white circle) in each plot indicates the crystallographic direction of the maximum (minimum) value.

In contrast to the $P4_2/mnm$ and $Pbcn$ phases, the P-phase hosts a drastically different sound-velocity profile [Fig. 5(c)]. Its fastest and slowest V_P are 10.99 km/s in the $\langle 001 \rangle$ direction and 10.76 km/s in the $\langle 221 \rangle$ direction, respectively, with an AV_P of 2.1 %. The maximum AV_S of the P-phase is 5.27%, a sixfold reduction compared to the $Pbcn$ phase. These significant differences may be attributed to the different underlying crystal structures. Although the $Pbcn$ and P-phase are both octahedrally coordinated, the $Pbcn$ phase at 41 GPa contains three pairs of nonequivalent Fe-O bonds with bond lengths between 1.7833 and 1.9052 Å. In contrast, the P-phase at 81 GPa is sixfold coordinated with all equivalent Fe-O bonds of a uniform bond length 1.7822 Å. This bonding difference drastically reduces the sound-velocity anisotropies and leads to very different sound-velocity profiles. These results highlight large variations in the elastic response and the resulting sound velocity behavior in various FeO_2 phases at different pressures, which provide insights for interpreting the seismic signatures of these FeO_2 phases.

VI. CONCLUSIONS

Our study establishes thermodynamic stability of recently synthesized P-phase FeO_2 at pressures above 74 GPa and, more importantly, unveils two metastable FeO_2 phases in $P4_2/mnm$ and $Pbcn$ symmetries, respectively, as validated by an excellent match of simulated and measured XRD spectra in the decompression products of P-phase FeO_2. An analysis of the lattice vibration of P-phase FeO_2 uncovers a soft mode associated with a rigid rotation of the FeO_6 octahedra. This libration mode stems from a shallow potential energy surface along the O-O bond connecting adjacent FeO_6 octahedra, rendering its length highly sensitive to computational and actual physical environments. The resulting large bond-length variation makes it inconsistent and unreliable to determine the Fe oxidation state based solely on the O-O bond length. We therefore have pursued a series of alternative approaches based on ELF, Bader charge, and COHP calculations, and the results collectively provide strong evidence characterizing P-phase FeO_2 as a peroxide while assigning Fe a valence state between +2 and +3. We further computed sound velocities of the newly discovered FeO_2 phases. The results agree well with recent experimental data on P-phase FeO_2 and reveal very different sound-velocity profiles in two metastable phases, showcasing their distinct seismic signatures. The present findings advance fundamental understanding of structural, bonding, and elastic properties of iron oxide FeO_2 phases, offering insights for assessing and interpreting their seismic signatures.

ACKNOWLEDGMENTS

We thank Professor R. Hoffmann for valuable discussions. C.L. acknowledges Dr. Q. Hu for providing the unpublished experimental XRD data of FeO_2 at 31 and 41 GPa. C.L. and C.F.C. acknowledge financial support from the U. S. Department of Energy under Cooperative Agreement Grant No. DE-NA0001982. M.A. acknowledges financial support from the Novartis Universität Basel Excellence Scholarship for Life Sciences and the Swiss National Science Foundation (Projects No. P300P2-158407 and No. P300P2-174475). The computational resources from the Swiss National Supercomputing Center in Lugano (Projects s700), the Extreme Science and Engineering Discovery Environment (XSEDE), which is supported by National Science Foundation Grant No. OCI-1053575, the Bridges system at the Pittsburgh Supercomputing Center (PSC), which is supported by NSF Award No. ACI-1445606, the Quest high performance computing facility at Northwestern University, and the National Energy Research Scientific Computing Center (Grant No. DE-AC02-05CH11231), are gratefully acknowledged.

[1] K. Otsuka and S. Karato, Nature (London) **492**, 243 (2012).
[2] M. S. Senn, J. P. Wright, and J. P. Attfield, Nature (London) **481**, 173 (2012).
[3] G. L. Weerasinghe, C. J. Pickard, and R. J. Needs, J. Phys.: Condens. Matter **27**, 455501 (2015).
[4] Q. Y. Hu, D. Y. Kim, W. G. Yang, L. X. Yang, Y. Meng, L. Zhang, and H. K. Mao, Nature (London) **534**, 241 (2016).
[5] J. Liu, Q. Y. Hu, D. Y. Kim, Z. Q. Wu, W. Z. Wang, Y. M. Xiao, P. Chow, Y. Meng, V. B. Prakapenka, H. K. Mao, and W. L. Mao, Nature (London) **551**, 494 (2017).
[6] Y. W. Fei and H. K. Mao, Science **266**, 1678 (1994).
[7] A. Sanson, I. Kantor, V. Cerantola, T. Irifune, A. Carnera, and S. Pascarelli, Phys. Rev. B **94**, 014112 (2016).
[8] N. N. Su, Y. H. Han, Y. Z. Ma, H. W. Liu, B. H. Ma, and C. X. Gao, Appl. Phys. Lett. **99**, 211902 (2011).
[9] Y. Ding, D. Haskel, S. G. Ovchinnikov, Y. C. Tseng, Y. S. Orlov, J. C. Lang, and H. K. Mao, Phys. Rev. Lett. **100**, 045508 (2008).
[10] B. Lavina, P. Dera, E. Kim, Y. Meng, R. T. Downs, P. F. Weck, S. R. Sutton, and Y. S. Zhao, Proc. Natl. Acad. Sci. U. S. A. **108**, 17281 (2011).

[11] B. Lavina and Y. Meng, Sci. Adv. **1**, e1400260 (2015).

[12] E. Bykova, L. Dubrovinsky, N. Dubrovinskaia, M. Bykov, C. McCammon, S. V. Ovsyannikov, H. P. Liermann, I. Kupenko, A. I. Chumakov, R. Rüffer *et al.*, Nat. Commun. **7**, 10661 (2016).

[13] B. G. Jang, D. Y. Kim, and J. H. Shim, Phys. Rev. B **95**, 075144 (2017).

[14] S. S. Streltsov, A. O. Shorikov, S. L. Skornyakov, A. I. Poteryaev, and D. I. Khomskii, Sci. Rep. **7**, 13005 (2017).

[15] A. J. Bridgeman and J. Rothery, J. Chem. Soc. Dalton Trans. **22**, 4077 (1999).

[16] J. P. Collman, R. R. Gagne, C. A. Reed, W. T. Robinson, and G. A. Rodley, Proc. Natl. Acad. Sci. U. S. A. **71**, 1326 (1974).

[17] Y. C. Wang, J. Lv, L. Zhu, and Y. M. Ma, Phys. Rev. B **82**, 094116 (2010).

[18] Y. C. Wang, J. Lv, L. Zhu, and Y. M. Ma, Comput. Phys. Commun. **183**, 2063 (2012).

[19] J. Lv, Y. C. Wang, L. Zhu, and Y. M. Ma, Phys. Rev. Lett. **106**, 015503 (2011).

[20] L. Zhu, H. Y. Liu, C. J. Pickard, G. T. Zou, and Y. M. Ma, Nat. Chem. **6**, 644 (2014).

[21] L. Zhu, H. Wang, Y. C. Wang, J. Lv, Y. M. Ma, Q. L. Cui, Y. M. Ma, and G. T. Zou, Phys. Rev. Lett. **106**, 145501 (2011).

[22] Y. W. Li, J. Hao, H. Y. Liu, Y. L. Li, and Y. M. Ma, J. Chem. Phys. **140**, 174712 (2014).

[23] H. Wang, J. S. Tse, K. Tanaka, T. Iitaka, and Y. M. Ma, Proc. Natl. Acad. Sci. U. S. A. **109**, 6463 (2012).

[24] D. Zhou, Q. Li, Y. M. Ma, Q. L. Cui, and C. F. Chen, J. Phys. Chem. C **117**, 5352 (2013).

[25] Q. Li, D. Zhou, W. T. Zheng, Y. M. Ma, and C. F. Chen, Phys. Rev. Lett. **110**, 136403 (2013).

[26] M. Zhang, H. Y. Liu, Q. Li, B. Gao, Y. C. Wang, H. D. Li, C. F. Chen, and Y. M. Ma, Phys. Rev. Lett. **114**, 015502 (2015).

[27] Q. Li, D. Zhou, W. T. Zheng, Y. M. Ma, and C. F. Chen, Phys. Rev. Lett. **115**, 185502 (2015).

[28] D. Zhou, Q. Li, W. T. Zheng, Y. M. Ma, and C. F. Chen, Phys. Chem. Chem. Phys. **19**, 4560 (2017).

[29] C. Lu, Q. Li, Y. M. Ma, and C. F. Chen, Phys. Rev. Lett. **119**, 115503 (2017).

[30] G. Kresse and J. Furthmüller, Phys. Rev. B **54**, 11169 (1996).

[31] P. E. Blöchl, Phys. Rev. B **50**, 17953 (1994).

[32] H. J. Monkhorst and J. D. Pack, Phys. Rev. B **13**, 5188 (1976).

[33] A. Togo, F. Oba, and I. Tanaka, Phys. Rev. B **78**, 134106 (2008).

[34] R. F. W. Bader, *Atoms in Molecules: A Quantum Theory* (Oxford University Press, Oxford, 1994).

[35] R. Dronskowski and P. E. Blöchl, J. Phys. Chem. **97**, 8617 (1993).

[36] V. I. Anisimov, I. V. Solovyev, M. A. Korotin, M. T. Czyżyk, and G. A. Sawatzky, Phys. Rev. B **48**, 16929 (1993).

[37] J. P. Perdew, K. Burke, and M. Ernzerhof, Phys. Rev. Lett. **77**, 3865 (1996).

[38] L. Wang, T. Maxisch, and G. Ceder, Phys. Rev. B **73**, 195107 (2006).

[39] Q. Y. Hu, D. Y. Kim, J. Liu, Y. Meng, L. X. Yang, D. Z. Zhang, W. L. Mao, and H. K. Mao, Proc. Natl. Acad. Sci. U. S. A. **114**, 1498 (2017).

[40] Y. M. Ma, A. R. Oganov, and C. W. Glass, Phys. Rev. B **76**, 064101 (2007).

[41] K. Parlinski, Z. Q. Li, and Y. Kawazoe, Phys. Rev. Lett. **78**, 4063 (1997).

[42] D. Mainprice, Comput. Geosci. **16**, 385 (1990).

[43] P. Porta, J. P. Remeika, M. Marezio, and P. D. Dernier, Mater. Res. Bull. **7**, 157 (1972).

[44] A. A. Bolzan, C. Fong, B. J. Kennedy, and C. J. Howard, Aust. J. Chem. **46**, 939 (1993).

[45] See Supplemental Material at http://link.aps.org/supplemental/10.1103/PhysRevB.98.054102 for details on the calculated pressure-volume relations, structural data, electronic properties, and sound velocities of FeO_2 at high pressure, the calculated Bader's charge of typical iron oxides, peroxides, monoxides, and dioxides.

[46] R. L. Tallman, J. L. Margrave, and S. W. Bailey, J. Am. Chem. Soc. **79**, 2979 (1957).

[47] A. A. Bolzan, C. Fong, B. J. Kennedy, and C. J. Howard, Acta Crystallogr., Sect. B **53**, 373 (1997).

[48] M. S. Miao, R. Hoffmann, J. Botana, I. I. Naumov, and R. J. Hemley, Angew. Chem. Int. Ed. **129**, 992 (2017).

[49] M. S. Miao and R. Hoffmann, J. Am. Chem. Soc. **137**, 3631 (2015).

[50] M. S. Miao, Nat. Chem. **5**, 846 (2013).

[51] S. Lafuerza, J. García, G. Subías, J. Blasco, J. Herrero-Martín, and S. Pascarelli, Phys. Rev. B **90**, 245137 (2014).

[52] A. Savin, O. Jepsen, J. Flad, O. K. Andersen, H. Preuss, and H. G. Vonschnering, Angew. Chem. Int. Ed. **31**, 187 (1992).

[53] M. Wuttig, D. Lüsebrink, D. Wamwangi, W. Welnic, M. Gillessen, and R. Dronskowski, Nat. Mater. **6**, 122 (2007).

[54] T. Zeng, R. Hoffmann, R. Nesper, N. W. Ashcroft, T. A. Strobel, and D. M. Proserpio, J. Am. Chem. Soc. **137**, 12639 (2015).

[55] X. D. Wen, T. J. Cahill, and R. Hoffmann, J. Am. Chem. Soc. **131**, 2199 (2009).

[56] M. Rahm, R. Hoffmann, and N. W. Ashcroft, J. Am. Chem. Soc. **139**, 8740 (2017).

[57] J. F. Lin, W. Sturhahn, J. Y. Zhao, G. Y. Shen, H. K. Mao, and R. J. Hemley, Science **308**, 1892 (2005).